Kinetic Growth Regimes of Hydrothermally Synthesized Potassium Tantalate Nanoparticles

Tiffany Ly,[†] Jianguo Wen,[‡] and Laurence D. Marks[*,†]

[†]Department of Materials Science and Engineering, Northwestern University, Evanston, Illinois 60208, United States
[‡]Center for Nanoscale Materials, Argonne National Laboratory, Lemont, Illinois 60439, United States

S Supporting Information

ABSTRACT: A general mathematical kinetic growth model is proposed on the basis of observed growth regimes of hydrothermally synthesized KTaO$_3$ nanoparticles from electron microscopy studies on the surface morphology and surface chemistry. Secondary electron imaging demonstrated that there are two dominant growth mechanisms: terrace nucleation, where the surfaces are rough, and terrace growth, where surfaces are smooth. In the proposed model based upon standard step-flow growth, the rates of both mechanisms are established to be dependent on the chemical potential change of the growth environment—terrace nucleation dominates with larger negative chemical potential, and terrace growth dominates with smaller negative chemical potential. This analysis illustrates the importance of ending a synthesis in a regime of low negative chemical potential in order to achieve smooth well-faceted nanoparticles.

KEYWORDS: Nanoparticles, kinetics, growth, synthesis, model, surfaces, shape
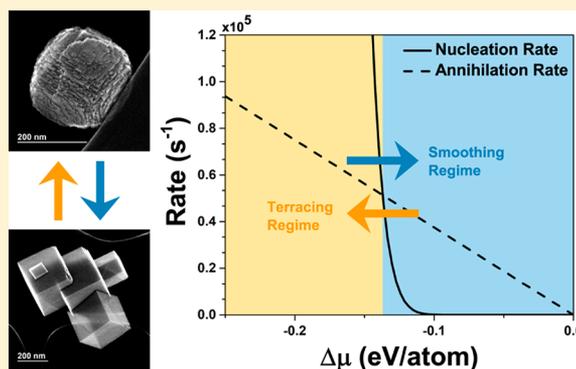
Nanoparticles play an increasingly important role in many fields, making the synthesis of nanoparticles vital to many areas of scientific research, including catalysis and electronics. In some cases, the interest in synthesis is restricted to producing small sizes alone, but in most cases, one wants to venture beyond this to obtain control over the shape of nanoparticles—in both broad features, such as shape aspect ratio, as well as fine details, such as surface growth terrace concentrations or morphology and atomic arrangements. In some cases, classic continuum models such as the thermodynamic and kinetic Wulff constructions have been used to understand nanoparticle shapes.[1−3] Another approach is to use atomistic approaches such as molecular dynamics.[4,5] While these approaches can be very powerful, it is not always clear how analyses from one specific material can be generalized to produce design rules with wider relevance. One issue is that many of the important parameters, such as surface chemistry, structure, and growth terrace densities, are frequently difficult to reliably determine from experiment or theory.

As recently reviewed,[6] three processes occur simultaneously during the nucleation and kinetic growth of nanoparticles: (1) nucleation of particles, (2) nucleation of terraces on particle surfaces, and (3) lateral growth of terraces. The rates of all three of these processes can affect many different properties of the product, including size distribution, shape, and surface morphology. However, controlling these rates is a complex problem; they each depend on a large variety of variables, such as temperature, pressure, volume, and

concentration of reagents. Nanoparticle syntheses are often further complicated by the addition of surfactants, which alter surface energies and growth kinetics. Ideally, the contribution of each variable should be individually studied for a more complete understanding.

Potassium tantalate, an incipient ferroelectric, is an oxide material of interest for many applications due to its unique properties.[7] Studies have shown its potential as a tunable microwave element[8−10] and as a photocatalyst for water splitting.[11−13] It has been synthesized using several techniques, including solvothermal methods,[12,14] hydrothermal syntheses,[15−18] supercritical syntheses,[11] and solid-state reactions.[8,13] The simple hydrothermal synthesis used herein is composed of only two reagents and lacks the addition of surfactants, making it easier to distinguish the effects of different variables on nanoparticle growth kinetics.

In this work, X-ray diffraction (XRD) and electron microscopy are used to analyze and characterize the kinetics of hydrothermally synthesized KTaO$_3$ nanoparticle growth. By analyzing the surface morphology over time, two different growth regimes were identified; the terrace nucleation rate dominates in the first regime, and terrace growth dominates in the second. Analysis of the resulting data is supported by a mathematical model developed to describe the two kinetic

growth regimes. High resolution transmission electron microscopy provided further insight into the role of different chemical species during nucleation and growth by characterizing the surface chemistry and structure.

The hydrothermal synthesis of $KTaO_3$ nanoparticles used was based on that described by Goh et al.[15] We added 0.0025 mol of L-Ta_2O_5 powder (1.1 g) and 25 mL of 15 M KOH solution to a 125 mL Teflon-lined autoclave. The autoclave was then heated to 150 °C for 1−4 h, and the product was washed and centrifuged with deionized water several times. The resulting white powder was dried overnight at 80 °C. To prepare samples for scanning and high resolution transmission electron microscopy (STEM and HRTEM), the powder was dispersed in ethanol and drop cast onto lacey carbon coated grids.

Powder X-ray diffraction was performed on a Rigaku DMAX diffractometer equipped with a Cu Kα source operated at 40 kV and 20 mA. The diffraction patterns were matched to compounds using the MDI JADE data analysis program,[19] and the phase fraction of each compound for each pattern was quantified by Rietveld refinement.

Secondary electron (SE) imaging was performed on a Hitachi HD-2300 STEM operated at 200 kV. To determine areal growth terrace densities, the SE images were analyzed using stereology, where a linear probe was used to extract random and statistical measurements of the terrace areal densities from the SE images.[20] This was done by moving a line (the linear probe) across an image and counting every instance where the line intersected with a terrace (Figure S1). The linear probe prevented bias in measurements by aiding the eye in counting intersections only.

HRTEM was performed on the Argonne chromatic aberration-corrected transmission electron microscope (ACAT), an FEI Titan 80-300 ST equipped with a CEOS C_c/C_s corrector at Argonne National Laboratory, to characterize the nanoparticle surfaces with profile imaging.[21−25] In order to interpret image contrast, HRTEM images were simulated using the MacTempasX software package,[26] which uses the multislice method[27] and nonlinear imaging theory.[28]

We will first describe the general crystallography of the nanoparticles and the general growth kinetics, before examining in more detail the atomic scale features such as terrace densities. After this, results on the surface chemistry will be presented.

Growth Kinetics and Surface Morphology. Powder XRD patterns taken of the products after 1−4 h of synthesis time are shown in Figure 1. The XRD patterns were indexed to match L-Ta_2O_5 (PDF 00-025-0922) and $KTaO_3$ (PDF 04-005-7249). The yield of $KTaO_3$ over time was calculated from these XRD patterns using Rietveld refinement, as shown in Figure 2a (see details in Table S1). On the basis of the observed diffraction peaks and quantification of the diffraction patterns, the reactants are almost completely (∼94 mol %) converted to $KTaO_3$ after 2 h. Although the assumptions of the Johnson−Mehl−Avrami−Kolmogorov (JMAK) equation were not satisfied in this synthesis,[29−32] the reaction yield can be fit to the functional form of JMAK to analyze changes in the kinetics of the growth processes, i.e.,

$$x = 1 - e^{-kt^m} \tag{1}$$

where x is the fraction of product yielded at time t, k is a rate constant, and m is a constant that provides information about the growth process. If this is plotted in the form $\ln(-\ln(1 - x))$
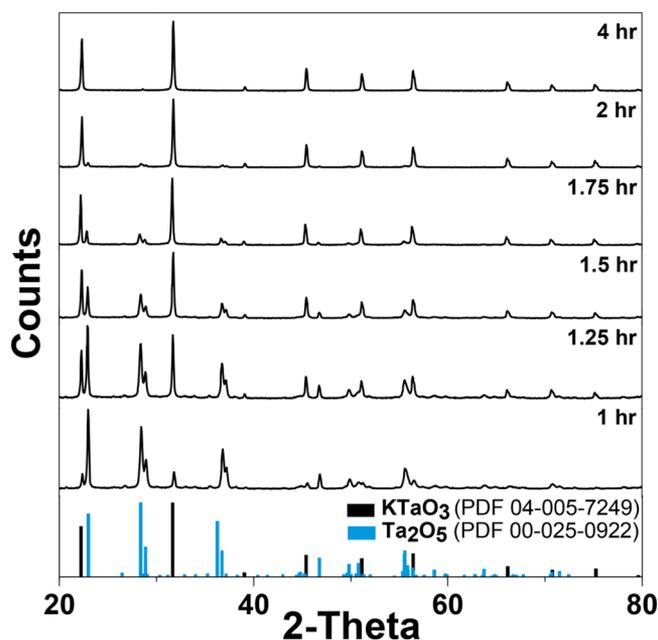

Figure 1. XRD patterns of the hydrothermal synthesis products at different time steps between 1 and 4 h of synthesis. Between 1 and 2 h, the patterns show signals from both the reagent L-Ta_2O_5 (blue bars, PDF 00-025-0922) and the product $KTaO_3$ (black bars, PDF 04-005-7249). At 2 h, the conversion to $KTaO_3$ is almost complete, and by 4 h, the product consists of only $KTaO_3$.
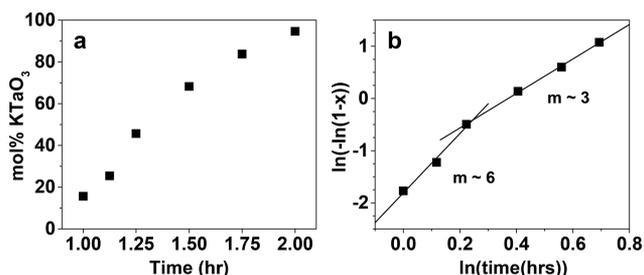
Figure 2. (a) Yield of $KTaO_3$ in mol % after different lengths of synthesis time. Yield was calculated with Rietveld refinement. (b) Logarithmic plot of the yield showing two linear fits with slopes of ∼6 and ∼3.

as a function of ln t, linear functions may be fit to the data with slopes m. This analysis is shown in Figure 2b for the time period between 1 and 2 h. The period 1−2 h was chosen for this analysis because the system underwent an incubation period before 1 h, and the reaction was almost complete after 2 h. This data was well described by two linear fits—one for 1−1.25 h where $m \sim 6$ and one for 1.25−2 h where $m \sim 3$, suggesting two different growth regimes. We will return later to explain the source of the two slopes.

Turning next to details of the nanoparticles, Figure 3 shows SE images of the samples, which were ∼200 nm sized cuboids. The surface morphology of the nanoparticles evolved over time. Between 1 and 1.75 h, the nanoparticle facets were populated with many growth terraces, giving a relatively rough appearance. After 2 h of growth, the facets appeared smooth and resembled the final product imaged after 4 h. The heights of the terraces were on the order of 1−3 unit cells of bulk $KTaO_3$.
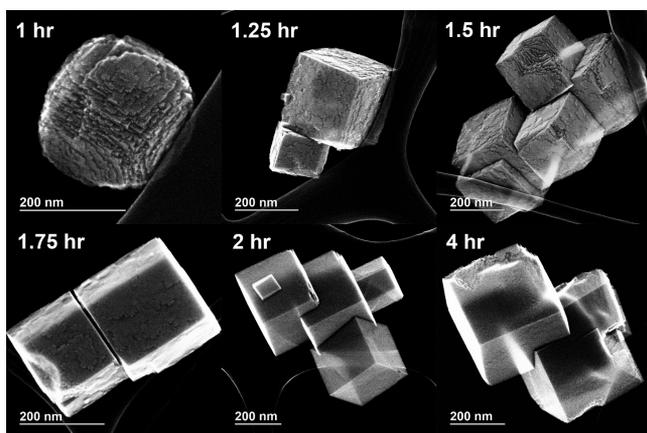
Figure 3. SE images of the KTaO₃ nanoparticles after 1−4 h of hydrothermal synthesis. Images show nanocuboids ~200 nm in size with sharp corners and edges.

The areal density distribution of terraces on the nanoparticle surfaces was measured for each time step between 1 and 1.75 h. The 2 h time step was excluded here because the surfaces appeared completely smooth. These plots demonstrate that the areal density of terraces, or roughness, decreased with time, while the distribution also narrowed. A size distribution of the nanoparticles for each time step between 1 and 2 h is provided in Figure 4b. In contrast to the terrace density, the size distribution broadened and the average size increased as the synthesis progressed until 2 h, where the average size decreased.
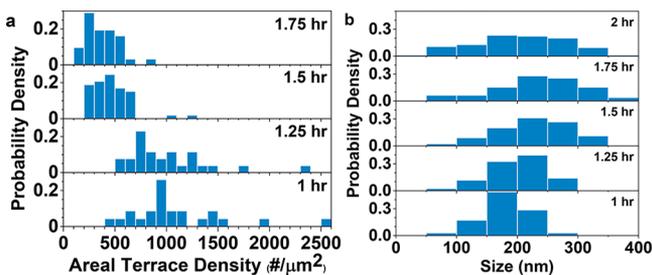
Figure 4. (a) Histogram of areal terrace density measured on nanoparticle facets for 1, 1.25, 1.5, and 1.75 h hydrothermal synthesis products. Histograms show narrowing distributions and decreasing densities with time. (b) Nanoparticle size distribution for synthesis times between 1 and 2 h. Distributions broaden with increasing time, and the average size increases with increasing time until 2 h, where the average size begins to decrease. (See enlarged plots in Figure S2.)

Surface Chemistry. We now turn to a description of results on the surface chemistry, which will be needed later when a general model for the growth is described. A high resolution profile image of the 4 h nanoparticles oriented along the [1 1 0] zone axis is shown in Figure 5a. The surface 1−2 nm of the nanoparticles showed an approximately uniformly distributed phase with differing structure and lattice spacing than bulk KTaO₃. There was also some structural disorder in the region between the surface and the bulk, which may be attributed to overlapping terraces of the nanoparticle and mismatch between the surface phase and the bulk phase. Similar features were also observed on the 1 h nanoparticles (Figure S3). When the electron beam intensity was over a dose rate of 100 e⁻/nm² s, a beam damage effect was observed, as
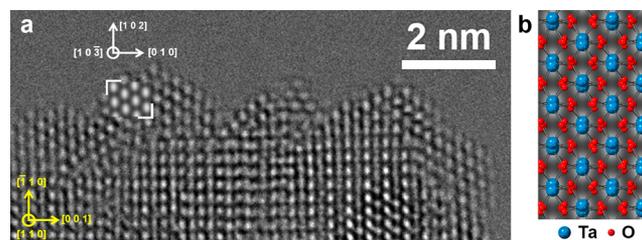
Figure 5. (a) Profile-view HRTEM image (with a dose rate of 30 e⁻/nm² s) of a 4 h KTaO₃ nanoparticle oriented along the [1 1 0] zone with a multislice simulation of B-Ta₂O₅ inset (white brackets). (b) Image simulation of B-Ta₂O₅ with the atomic structure superimposed, where large blue atoms are Ta and small red atoms are O.

shown in Figure S4.[33] Images of areas with well-ordered structures and little evidence of beam damage (i.e., with beam intensity below 100 e⁻/nm²s) were considered to determine the surface chemistry. To interpret the contrast of images and investigate possible structure matches for the surface, multislice HRTEM simulations were performed mimicking the microscope conditions using several different structures to match the contrast and periodicity of these regions. A range of possible structures were considered; taking into account that both the precursors and KTaO₃ contain Ta⁵⁺ and no reductants were used, only phases containing Ta⁵⁺ were chemically reasonable, i.e., potassium tantalate, tantalum(V) oxide, and tantalum(V) hydroxide. The structures were further narrowed on the basis of energy dispersive X-ray spectroscopy data that suggested the surfaces were potassium deficient and tantalum rich (Figure S5). Of the possibilities, B-Ta₂O₅, a high-pressure polymorph of tantalum oxide belonging to space group 15 (C2/c),[34] was the best match. A multislice simulation of B-Ta₂O₅ oriented along the [1 0 3̄] zone axis is shown as an inset in Figure 5a (white brackets). Figure 5b shows the B-Ta₂O₅ atomic structure superimposed on the image simulation, where bright spots correspond to Ta atoms (blue) and dark spots correspond to O atoms (red). There is a lattice mismatch between the simulated B-Ta₂O₅ and bulk KTaO₃ of approximately 7 and −9% along the [1 0 3̄] and [0 1 0] directions, respectively. While this mismatch is relatively large, such values for a very thin surface region are not unreasonable.

This misfit strain may also partially explain why the high-pressure B-Ta₂O₅ phase terminates the surface as opposed to the low temperature phase, L-Ta₂O₅.[35] Epitaxial strain stabilization of nonequilibrium stable phases has been demonstrated in many different cases including oxide thin films.[36,37] We note that the published L-Ta₂O₅ phase has longer bond lengths and did not match the experimental images (Figure S6). The literature reports the B-Ta₂O₅ phase to be only stable at high temperatures and pressures.[34] It has also been hydrothermally synthesized under pressure and temperature conditions of 20 MPa and 570 K.[38] Both reports demonstrated that the B-Ta₂O₅ phase is metastable at room temperature. Even though the reported syntheses of B-Ta₂O₅ were performed at higher temperatures and pressures than detailed here, we show in the Supporting Information that these conditions are still reasonable for forming this high temperature and pressure phase.

The experimental results and the slope change in Figure 2 indicated that there were two growth regimes, an overall evolution over time of the surface morphology from rough

surfaces with a high terrace density to smooth surfaces as well as an excess of Ta_2O_5 at the surface in the form of a high temperature and pressure stable structure, which has a good epitaxial and tantalum coordination match to the $KTaO_3$ substrate. We will now show how these results can be understood in terms of a general growth model based upon conventional step-flow growth.

Growth Model. The appearance of terraces on the nanoparticle surfaces and subsequent smoothing is indicative of kinetic growth processes. After nucleation, the growth of nanoparticles occurred in two stages: (1) nucleation of terraces on nanoparticle surfaces and (2) lateral growth of terraces. Before proceeding to model the rates of these two processes, it is important to define several terms. The change in chemical potential ($\Delta\mu$) per molecule added to the nanoparticle is dependent on the chemical potential difference between the initial reactant species (Ta_2O_5 and KOH) and the final product ($KTaO_3$). As it is a driving force for a reaction to proceed, $\Delta\mu$ must be negative, so we will be interested in how largely negative $\Delta\mu$ would be during a reaction. $\Delta\mu$ can vary with many factors, including reagent concentration, temperature, pressure, and volume. In this synthesis, since the molar ratio of the reagents KOH:Ta_2O_5 is 150:1, the concentration of KOH can be considered constant as a function of time. Given the incubation period of 1 h, it was also assumed that the species were sufficiently mixed so that the overall $\Delta\mu$ was not affected by dissolution rates and concentration distributions. Furthermore, because the hydrothermal synthesis was performed at a constant temperature and pressure in a closed vessel of fixed volume, these variables may also be considered constant. Thus, $\Delta\mu$ primarily varied with the concentration of Ta_2O_5, which decreases over time as the reaction yield increases (Figure 2a), meaning that $\Delta\mu$ became less negative over time. A direct relationship between $\Delta\mu$ and the Ta_2O_5 concentration was difficult to calculate under the circumstances because the reaction took place in a sealed autoclave under relatively high temperature and pressure, which prevented the direct study of the solute species present, the free energies of those species during the reaction, the exact chemical reaction mechanisms occurring, and the specific thermodynamic conditions of the system. As also mentioned earlier, and will become clearer below, there are other specific numbers for which only reasonable estimates are possible at present, for instance, step energies in solution at elevated temperature and pressure. However, in this case, the specific solutes present and any intermediate reactions occurring are of little consequence compared to the overall reaction from the initial reactants to the final product, which is the reaction that results in the growth of nanoparticles. This overall reaction generates the effective $\Delta\mu$, the relative value of which may be reasonably related to the concentration of Ta_2O_5 given the assumptions made above.

The results of the HRTEM characterization and multislice simulations provided further evidence that the concentration of the Ta_2O_5 controls the kinetics of the nanoparticle synthesis. Figure 5 demonstrates that the surface of the $KTaO_3$ is terminated by B-Ta_2O_5, a tantalum oxide phase rather than a potassium tantalate phase, which has been observed in other $KTaO_3$ surface studies.[39,40] Because the surfaces of the nanoparticles are terminated with a Ta_2O_5 phase, this suggests that the tantalum species in solution was a major factor in controlling $\Delta\mu$ during the reaction.

The terrace nucleation and growth rates may be modeled using mathematical functions dependent on $\Delta\mu$. In standard growth formulations, the nucleation rate of terraces is an exponential function (e.g., ref 6 and references therein as well as the Supporting Information)

$$N_R = f_0 \exp\left(-\frac{\Delta E}{k_B T}\right) \tag{2}$$

$$\Delta E = \frac{-\pi(N_E\gamma_e)^2}{N_S\Delta\mu} \tag{3}$$

where N_R is the nucleation rate, f_0 is the frequency factor, ΔE is the activation energy, k_B is the Boltzmann constant, and T is the temperature. As shown in eq 3, where γ_e is the step edge energy per atom, N_E is the number of atoms per unit length of a terrace, and N_S is the number of atoms per unit area of a terrace, the activation energy ΔE is inversely proportional to $\Delta\mu$. In contrast, the rate of growth (G_R) is linearly dependent on $\Delta\mu$[41−43]

$$G_R = C\Delta\mu \tag{4}$$

where C is a coefficient dependent on a variety of factors, including the concentration gradient of reactant species in the solution, diffusivity, pressure, and temperature. When a terrace grows across a facet and reaches the edges, it is annihilated. The rate of annihilation (A_R) is proportional to the growth rate of terraces

$$A_R = \frac{1}{A}G_R \tag{5}$$

where A is the size of the specific nanoparticle face.

Because both the terrace nucleation rate and annihilation rate are dependent on $\Delta\mu$, they will intersect at a value $\Delta\mu_{critical}$, which is where the dominating growth process switches. Equations 2 and 5 were simulated as a function of $\Delta\mu$ for a reaction temperature of 150 °C and a nanoparticle facet size of 200 nm. Parts a and c of Figure 6 show these simulations using γ_e of 0.4 and 0.2 eV/atom, respectively, to demonstrate how $\Delta\mu_{critical}$ is related to the material being grown. Generally, $\Delta\mu_{critical}$ will be on the same order of γ_e, which was estimated for these plots using known values in the literature for similar materials (see the Supporting Information). The yellow shaded regions indicate the terracing regime at more negative $\Delta\mu$, which is where nucleation of terraces will dominate. At less negative $\Delta\mu$, terrace growth and annihilation will dominate, as indicated by the blue shaded regions. As discussed earlier, $\Delta\mu$ became less negative as the synthesis of $KTaO_3$ progressed, which meant that it moved from left to right in the plot of Figure 6a—moving from the terracing regime to the smoothing regime, as observed in Figure 3. While the exact value of $\Delta\mu$ cannot be calculated for this particular synthesis, the most important relationship is where $\Delta\mu$ is relative to $\Delta\mu_{critical}$, thereby determining which growth mechanism dominates.

The transition between the two growth regimes is also dependent on the nanoparticle size because the annihilation rate increases with decreasing nanoparticle facet area, as well as the reaction temperature. Parts b and d of Figure 6 show $\Delta\mu_{critical}$ calculated for a series of reaction temperatures and nanoparticle sizes when γ_e is 0.4 and 0.2 eV/atom, respectively. $\Delta\mu_{critical}$ becomes more negative with decreasing temperature and nanoparticle size, widening the $\Delta\mu$ range where the
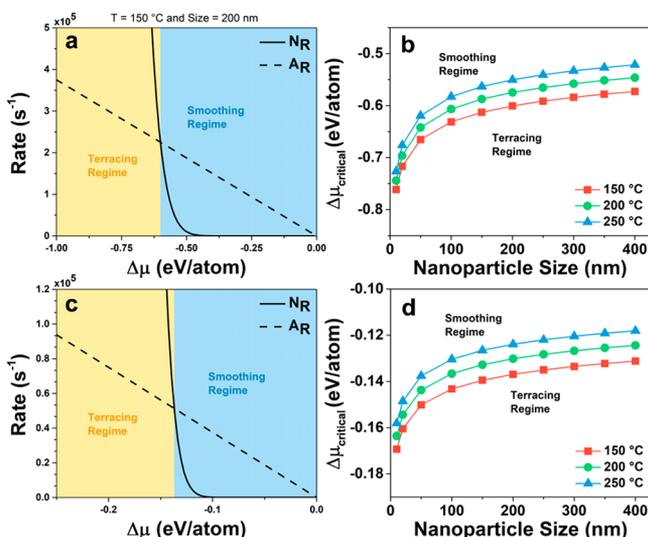
Figure 6. Terrace nucleation rate (solid) and annihilation rate (dashed) simulated as a function of $\Delta\mu$ for a reaction temperature of 150 °C and a nanoparticle size of 200 nm using estimated step energies of (a) 0.4 eV/atom and (c) 0.2 eV/atom (see the Supporting Information). The nucleation rate and annihilation rate intersect at $\Delta\mu_{critical}$, which is where the dominant growth regime switches between terrace nucleation (terracing regime) and terrace growth and annihilation (smoothing regime). Corresponding plots of $\Delta\mu_{critical}$ as a function of nanoparticle size for different synthesis temperatures with step energies of (b) 0.4 eV/atom and (d) 0.2 eV/atom.

smoothing regime will dominate. In contrast, with increasing temperatures and nanoparticle sizes, $\Delta\mu_{critical}$ increases, which increases the $\Delta\mu$ range where the terracing regime will dominate.

The model presented illustrates a case where the two processes, nucleation and growth of terraces, can dominate at different points during a synthesis due to changes in $\Delta\mu$. Therefore, by controlling $\Delta\mu$ during a synthesis, various properties of the product can be tuned, including surface morphology and size distribution. As evidenced by Figures 3, 4, and 6, nanoparticle surfaces can be relatively rough or smooth depending on which growth process is dominating. Under conditions of a greater negative $\Delta\mu$, when the nucleation of terraces is the prevailing process, nanoparticle surfaces will be rough. When $\Delta\mu$ is less negative, the nanoparticle surfaces will instead be smooth because the growth of terraces is dominant. Either surface morphology can be advantageous depending on the needs of an application. For example, nanoparticles with rougher surfaces can be beneficial for applications where high surface area is needed, as in catalysis.[44] Smooth, well-controlled surface and shapes are also important for identifying surface and shape dependent properties.[45]

In addition, the results shown in Figure 2b, where two lines were fit to the data, may be further elaborated by applying the proposed growth model. The two linear fits implied that there were two growth mechanisms with different kinetics during the synthesis of the nanoparticles and that the dominant mechanism changed where the slope changed from ~6 to ~3 at 1.25 h. This slope change may be correlated to moving from the terracing regime to the smoothing regime based upon the proposed growth model, suggesting that terrace nucleation was the dominant mechanism between 1 and 1.25 h and terrace growth dominated after 1.25 h.

Beyond the surface morphology, the size distribution of nanoparticles may also be affected by these growth processes. Typically, a monodisperse product may be achieved by increasing the nanoparticle nucleation rate at the beginning of the synthesis so that the nucleated particles grow at the same rate for the same length of time. However, Figure 4b demonstrates that the size distribution of the nanoparticles broadens with time. Furthermore, between 1.5 and 2 h, there is an increasing population of nanoparticles below 100 nm in size. The broadening size distribution may be attributed to the nucleation and growth rates and the two described growth regimes. As nucleated nanoparticles form at later time steps, they will remain small and smooth in appearance because the terrace growth process is dominating over the terrace nucleation process. Terrace nucleation is growth normal to nanoparticle surfaces, which will increase the nanoparticle size, whereas terrace growth is growth parallel to nanoparticle surfaces, which will instead smooth the surfaces. Therefore, to achieve monodisperse nanoparticles, it is not only important to nucleate most of the nanoparticles at the same time but also to isolate the regime where terrace growth dominates from the nanoparticle nucleation time period.

The proposed model may be used to better explain the observed behavior in other cases of hydrothermally synthesized perovskite oxide nanoparticles. By modifying the temperature and urea content in a reaction, Huang et al.[46] and Hou et al.[47] observed changes in both shape and faceting in $La_{0.5}Sr_{0.5}MnO_3$ and $LaCrO_3$. In both cases, increased terracing and decreased smoothing were observed in reactions performed at higher temperatures and with an increased amount of urea added. As shown in Figure 6, changes in temperature also change the value of $\Delta\mu_{critical}$, which affects the ranges of $\Delta\mu$ where the terracing and smoothing regimes may dominate. If a system previously residing in the smoothing regime (i.e., $\Delta\mu > \Delta\mu_{critical}$) experiences a temperature increase, the increase in temperature may shift $\Delta\mu_{critical}$ significantly enough such that $\Delta\mu < \Delta\mu_{critical}$, therefore moving the system into the terracing regime. This model suggests that increasing temperatures can move reactions toward the terracing regime. The addition of urea may also increase the magnitude of the chemical potential difference between the reactants and products, thereby further pushing the system into the terracing regime and resulting in rougher surfaces and less well-faceted nanoparticle surfaces.

The model may be used to inform synthesis design for producing smooth, well-faceted, and shape-controlled nanoparticles. In work to be published, efforts to produce well-faceted $LnScO_3$ nanoparticles have been facilitated by introducing to a previously developed synthesis[48] an initial growth step in the terracing regime at higher temperature, followed by a second growth step in the smoothing regime at lower temperature.[49] This sequence has successfully formed smooth and well-faceted $LnScO_3$ nanoparticles, which were previously unachievable in a single heating sequence (Figure S7).

In summary, a kinetic growth model of the terrace nucleation and growth regimes on nanoparticle surfaces based upon conventional growth theory is proposed from experimental observations and results of hydrothermally synthesized $KTaO_3$ nanoparticles. In this synthesis, the nanoparticles first undergo a regime of high terrace nucleation rate, followed by a regime of high terrace growth rate. The terrace growth dominant regime coincides with a regime where heterogeneous nucleation also dominates, resulting in smooth,

faceted nanoparticles. The balance of the terrace nucleation and growth rates can control many characteristics of the products, including the relative roughness or smoothness of the surfaces, how faceted the nanoparticles are, and the size distribution of the particles. The rates of the growth processes are dependent on the chemical potential change of the synthesis environment. By tuning the chemical potential difference through different synthesis variables, progress may move further in achieving size and shape controlled syntheses of nanoparticles.

■ ASSOCIATED CONTENT

Ⓢ Supporting Information

The Supporting Information is available free of charge on the ACS Publications website at DOI: 10.1021/acs.nano-lett.8b02123.

> Additional information about the terrace counting procedure, beam damaged samples, analytical electron microscopy results, other tantalum oxide structures considered, pressure conditions of growth, and estimated values used for the growth model (PDF)

■ AUTHOR INFORMATION

Corresponding Author
*E-mail: l-marks@northwestern.edu.

ORCID Ⓞ
Tiffany Ly: 0000-0002-8675-1467

Notes
The authors declare no competing financial interest.

■ ACKNOWLEDGMENTS

■ REFERENCES

(1) Wulff, G. Z. Kristallogr. Mineral. **1901**, 34 (5/6), 449−530.
(2) Sekerka, R. F. Cryst. Res. Technol. **2005**, 40 (4−5), 291−306.
(3) Frank, F. C. Growth and Perfection of Crystals; Wiley: New York, 1958.
(4) Zhang, H.; Banfield, J. F. Nano Lett. **2004**, 4 (4), 713−718.
(5) Zeng, Q.; Jiang, X.; Yu, A.; Lu, G. M. Nanotechnology **2007**, 18 (3), 035708.
(6) Marks, L. D.; Peng, L. J. Phys.: Condens. Matter **2016**, 28 (5), 053001.
(7) Nishihata, Y.; Kamishima, O.; Maeda, H.; Ishii, T.; Sawada, A.; Terauchi, H. Phys. B **1995**, 208−209, 311−312.
(8) Glinšek, S.; Malič, B.; Rojac, T.; Filipič, C.; Budič, B.; Kosec, M. J. Am. Ceram. Soc. **2011**, 94 (5), 1368−1373.
(9) Tagantsev, A. Appl. Phys. Lett. **2000**, 76 (9), 1182−1184.
(10) Vendik, O. G.; Hollmann, E. K.; Kozyrev, A. B.; Prudan, A. M. J. Supercond. **1999**, 12 (2), 325−338.
(11) Hayashi, H.; Hakuta, Y. J. Mater. Sci. **2008**, 43 (7), 2342−2347.
(12) He, Y.; Zhu, Y. Chem. Lett. **2004**, 33 (7), 900−901.
(13) Kato, H.; Kudo, A. Chem. Phys. Lett. **1998**, 295 (5−6), 487−492.
(14) Makarova, M.; Bykov, P.; Drahokoupil, J.; Cernansky, M.; Dlabacek, Z.; Dejneka, A.; Jastrabik, L.; Trepakov, V. Mater. Res. Bull. **2012**, 47 (7), 1768−1773.
(15) Goh, G. K. L.; Haile, S. M.; Levi, C. G.; Lange, F. F. J. Mater. Res. **2002**, 17 (12), 3168−3176.
(16) Gömpel, D.; Tahir, M. N.; Panthöfer, M.; Mugnaioli, E.; Brandscheid, R.; Kolb, U.; Tremel, W. J. Mater. Chem. A **2014**, 2 (21), 8033−8040.
(17) Hu, Y.; Gu, H.; Hu, Z.; Di, W.; Yuan, Y.; You, J.; Cao, W.; Wang, Y.; Chan, H. L. W. Cryst. Growth Des. **2008**, 8 (3), 832−837.
(18) Yun, B. K.; Koo, Y. S.; Jung, J. H.; Song, M.; Yoon, S. Phys. B **2010**, 405 (23), 4866−4870.
(19) MDI Jade, version 5.1.0; Materials Data: Livermore, CA, 2010.
(20) Hilliard, J. E.; Lawson, L. R. Stereology and Stochastic Geometry; Kluwer Academic Publishers: Dordrecht, The Netherlands; Boston, MA, 2003; p 488.
(21) Marks, L. D.; Smith, D. J. J. Cryst. Growth **1981**, 54 (3), 425−432.
(22) Marks, L. D.; Smith, D. J. Nature **1983**, 303, 316−317.
(23) Marks, L. D. Phys. Rev. Lett. **1983**, 51 (11), 1000−1002.
(24) Lin, Y.; Wen, J.; Hu, L.; Kennedy, R. M.; Stair, P. C.; Poeppelmeier, K. R.; Marks, L. D. Phys. Rev. Lett. **2013**, 111 (15), 156101.
(25) Crosby, L. A.; Kennedy, R. M.; Chen, B.; Wen, J.; Poeppelmeier, K. R.; Bedzyk, M. J.; Marks, L. D. Nanoscale **2016**, 8, 16606−16611.
(26) MacTempasX, version 2.3.44; Total Resolution: Berkeley, CA, 2014.
(27) Cowley, J. M.; Moodie, A. F. Acta Crystallogr. **1957**, 10, 609−619.
(28) O'Keefe, M. A. Proceedings of the 37th Annual Meeting of the Electron Microscopy Society of America, San Antonio, Texas, 1979; Claitor's Publicating Division: Baton Rouge, LA, 1979.
(29) Johnson, W. A.; Mehl, R. F. Trans. Am. Inst. Min., Metall. Pet. Eng. **1939**, 135, 416−442.
(30) Avrami, M. J. Chem. Phys. **1939**, 7 (12), 1103−1112.
(31) Avrami, M. J. Chem. Phys. **1940**, 8 (2), 212−224.
(32) Kolmogorov, A. N. Bull. Acad. Sci. URSS **1937**, 3, 355−359.
(33) Lin, Y.; Wen, J.; Hu, L.; McCarthy, J. A.; Wang, S.; Poeppelmeier, K. R.; Marks, L. D. Micron **2015**, 68, 152−157.
(34) Zibrov, I. P.; Filonenko, V. P.; Sundberg, M.; Werner, P.-E. Acta Crystallogr., Sect. B: Struct. Sci. **2000**, 56 (4), 659−665.
(35) Stephenson, N. C.; Roth, R. S. Acta Crystallogr., Sect. B: Struct. Crystallogr. Cryst. Chem. **1971**, 27, 1037−1044.
(36) Gorbenko, O. Y.; Samoilenkov, S. V.; Graboy, I. E.; Kaul, A. R. Chem. Mater. **2002**, 14, 4026−4043.
(37) Roy Chaudhuri, A.; Arredondo, M.; Hähnel, A.; Morelli, A.; Becker, M.; Alexe, M.; Vrejoiu, I. Phys. Rev. B: Condens. Matter Mater. Phys. **2011**, 84 (5), 054112.
(38) Izumi, F.; Kodama, H. J. Less-Common Met. **1979**, 63, 305−307.
(39) Koirala, P.; Gulec, A.; Marks, L. D. Surf. Sci. **2017**, 657, 15−19.
(40) Xu, Y. B.; Tang, Y. L.; Liu, Y.; Ma, X. L.; Zhu, Y. L. Philos. Mag. **2016**, 96 (5), 486−497.
(41) Levi, A. C.; Kotrla, M. J. Phys.: Condens. Matter **1997**, 9, 299−344.
(42) Bircumshaw, L. L.; Riddiford, A. C. Q. Rev., Chem. Soc. **1952**, 6 (2), 157−185.
(43) Burton, W. K.; Cabrera, N.; Frank, F. C. Philos. Trans. R. Soc., A **1951**, 243 (866), 299−358.
(44) Bell, A. T. Science **2003**, 299 (5613), 1688−1691.
(45) Nguyen, T. D. Nanoscale **2013**, 5 (20), 9455−9482.
(46) Huang, K.; Yuan, L.; Jiang, Y.; Zhang, J.; Geng, Z.; Luo, L.; Feng, S. Inorg. Chem. Front. **2018**, 5, 732−738.
(47) Hou, C.; Feng, W.; Yuan, L.; Huang, K.; Feng, S. CrystEngComm **2014**, 16 (14), 2874−2877.
(48) Paull, R. J.; Mansley, Z. R.; Ly, T.; Marks, L. D.; Poeppelmeier, K. R. Inorg. Chem. **2018**, 57, 4104−4108.
(49) Paull, R. J.; Ly, T.; Mansley, Z. R.; Poeppelmeier, K. R.; Marks, L. D. Manuscript in preparation, 2018.